Acta Biomaterialia 131 (2021) 391–402

Contents lists available at ScienceDirect

Acta Biomaterialia

journal homepage: www.elsevier.com/locate/actbio

Full length article

Microtensile failure mechanisms in lamellar bone: Influence of fibrillar orientation, specimen size and hydration

Daniele Casari[a,1,*], Tatiana Kochetkova[a], Johann Michler[a], Philippe Zysset[b], Jakob Schwiedrzik[a,*]

[a] EMPA-Swiss Federal Laboratories for Materials Science and Technology, Laboratory for Mechanics of Materials and Nanostructures, Thun 3602, Switzerland
[b] ARTORG Centre for Biomedical Engineering Research, University of Bern, Bern 3010, Switzerland

ARTICLE INFO

Article history:
Received 2 February 2021
Revised 17 June 2021
Accepted 18 June 2021
Available online 24 June 2021

Keywords:
Mineralized tissue
Fibrillar structure
Nanoscale
Toughening mechanisms
Strength
Crack initiation

ABSTRACT

A mechanistic understanding of bone fracture is indispensable for developing improved fracture risk assessment in clinics. Since bone is a hierarchically structured material, gaining such knowledge requires analysis at multiple length scales. Here, the tensile response of cortical bone is characterized at the lamellar length scale under dry and hydrated conditions with the aim of investigating the influence of bone's microstructure and hydration on its microscale strength and toughness. For individual lamellae, bone strength strongly correlates with the underlying mineralized collagen fibrils orientation and shows a 2.3-fold increase compared to the macroscale. When specimen size is increased to a few lamellae, the influence of fibril orientation and the size effect on strength are significantly reduced. These findings highlight the critical influence of defects, such as canaliculi and interlamellar interfaces, when assessing larger volumes. Hydration leads up to a 3-fold strength decrease but activates several toughening mechanisms enabling inelastic deformation. In axial specimens, toughening is seen through fibril bridging and crack kinking. In transverse specimens, water presence leads to a progressive but stable crack growth parallel to the fibril orientation, suggesting crack-tip plasticity at the fibrillar interfaces. This work offers a better understanding of the role of interfaces, porosity, and hydration in crack initiation under tensile loading, which is a crucial step towards improved clinical management of disease-related bone fractures through multiscale modeling approaches.

Statement of significance

Bone features a complex hierarchical structure which gives rise to several toughening mechanisms across several length scales. To better understand bone fracture, particularly the changes associated with age and disease, it is essential to investigate bone mechanical response at different levels of its hierarchical structure. For the first time, we were able to observe the nucleation of a single crack in hydrated bone lamellae under well-controlled uniaxial tensile loading conditions. These experiments highlight the role of water, interfaces, defects, and the ratio of defect to specimen size on bone's apparent strength and toughness. Such knowledge can be used in the future to develop multiscale models enabling improved clinical management of disease-related bone fractures.

1. Introduction

The increasing incidence of pathological fractures in aging societies constitutes a major health concern and calls for improved fracture risk assessment strategies [1]. Current assessment relies on bone mineral density, but factors such as material composition and microstructure also contribute to bone mechanical integrity [2,3]. Since bone exhibits a complex hierarchical structure, its

* Corresponding authors.
E-mail addresses: daniele.casari@epfl.ch (D. Casari), jakob.schwiedrzik@empa.ch (J. Schwiedrzik).
[1] Current address: Electron Spectrometry and Microscopy Laboratory, Swiss Federal Institute of Technology Lausanne, Switzerland.

https://doi.org/10.1016/j.actbio.2021.06.032
1742-7061/

fracture is inherently a multiscale process. Performing small-scale uniaxial tensile experiments at the tissue level can provide insights into crack initiation and growth in both healthy and diseased bone. A deeper understanding of bone fracture can ultimately lead to improved clinical management of disease-related bone fractures through multiscale modeling approaches [4]. To achieve this goal, it is first necessary to establish a thorough understanding of the underlying physical phenomena based on animal models of healthy bone. In a successive step, parameters such as age and disease should be included.

Bone's hierarchical structure spans several length scales. At the molecular scale, type-I collagen molecules (300 nm long, 1.5 nm wide) self-assemble into collagen fibrils (several μm in length, ~100 nm in diameter) [5,6]. Fibrils are gradually mineralized with thin elongated carbonated hydroxyapatite crystals (thickness: ~2–5 nm, length: 50 to 100 nm) [7]. The resulting mineralized collagen fibrils (MCFs) make up the elementary building blocks of bone [8,9]. MCFs are held together by an extrafibrillar matrix (EFM) of non-collagenous proteins (NCPs) and water. In mature human bone, parallel arrays of MCFs organize into plywood-like patterns to form thin (3–7 μm) lamellae [10–12]. In cortical bone, several lamellae concentrically encompass primary vascular canals and form secondary osteons (200–300 μm in diameter). These tubular structures are roughly oriented with the growth direction of bone and are often referred to as the structural units of cortical bone [13]. Despite its compact structure, cortical bone contains a network of vascular canals and hosts a complex cellular system: osteocytes are interconnected via 300 nm-wide canaliculi, forming the lacuno-canalicular network that regulates the transport of nutrients, biochemical signals, and hormonal stimuli [14]. Note that canaliculi are primarily oriented towards the osteon center [15]. While porosity leads to potentially significant stress concentrations, bone can counter fracture through multiple toughening mechanisms working in synergy across several length scales [16–18].

At the nanoscale, resistance to crack initiation and growth is governed by intrinsic toughening mechanisms that act in front of the crack tip, such as collagen uncoiling [19], intermolecular slip at mineral/collagen interface [20,21], and interfibrillar sliding via shearing of the EFM [22,23], which induces sacrificial bonds disruption [24–26], and microcracking [27–29]. At higher length scales (>1 μm), bone's toughness is dominated by extrinsic mechanisms that mainly operate in the wake of the crack and shield the latter from the applied driving force. Diffuse microcracking [30], crack deflection/twist at cement lines [31,32], and uncracked ligament bridging [33] are the most known extrinsic mechanisms in bone. While there is evidence that these mechanisms are controlled by interfaces and heterogeneities distributed throughout bone's hierarchical structure [34–37], a detailed description of bone fracture at different length scales is still missing, especially at the lamellar level. Recent studies have characterized the mechanical behavior of bone at the microscale via micropillar compression experiments [38–43]. Overall, these experiments showed a marked anisotropy associated with MCFs orientation [42], an important smaller-is-stronger size effect related to the sample-size scaling of the distribution of flaws [38,41], and highlighted a strong influence of hydration [39,42]. In single bone lamellae, plastic deformation and subsequent failure occurred due to shear planes at the weak interfaces or in the vicinity of pores [38]. Interestingly, at a lower length scale, in which only a couple of mineralized collagen fibrils are compressed, extrafibrillar shearing is inhibited, leading to brittle failure [41]. While these studies emphasize the scale-dependent behavior of bone, their findings might be only applicable to the compressive behavior of bone, which has been shown to differ significantly from the tensile behavior in terms of yield stress, post-yield behavior, and crack morphology [44,45].

In our recent work, the uniaxial microtensile properties of bone were characterized using a novel experimental setup [46]. However, experiments were limited to dry conditions, which is not representative of the physiological state of bone and led to premature brittle failure. So far, little is known about the microtensile properties of bone under hydrated conditions. Hydrated tensile experiments performed on fibrolamellar bone at the mesoscopic length scale (40–300 μm) revealed an inelastic response and an increased strength anisotropy compared to dry conditions [47]. A strong interaction of water with large weak interfaces is likely the cause for this behavior. Such marked anisotropy is in contrast with compression results in cortical bone at the lamellar length scale, for which strength anisotropy ratio remained constant in the presence of water [39].

In this study, we aimed to investigate how both microstructure and hydration affect the microscale anisotropic response of pristine lamellar bone (MCFs bundles that are not permeated by large voids such as osteocytes and microcracks) under uniaxial tension. Specimen size was kept in the order of a few lamellar units (5–20 μm). Focused ion beam (FIB) milled specimens were fabricated from ovine osteonal bone in axial and transverse orientations and successively tested in tension under both vacuum and hydrated conditions at quasi-static strain rates using a custom-made microtensile setup [48]. Material composition, fracture surfaces, and the underlying microstructure were assessed using Raman spectroscopy, high-resolution (HR) scanning electron microscopy (SEM), and scanning transmission electron microscopy (STEM), respectively. An overview of the study pipeline is illustrated in Fig. 1.

2. Experimental section

2.1. Microtensile specimen fabrication

An ovine tibia (3.5 years old) was obtained from a local abattoir. A 5 mm thick disk was cut from the center of its diaphysis and later sectioned into axial and transverse samples using a diamond-coated band saw (Exact, Germany). Samples were glued onto SEM stubs using cyanoacrylate glue (Ergo 5011, Switzerland), air-dried, and ultramilled (Polycut E, Reichert-Jung, Germany) to obtain smooth and flat surfaces. The axial sample was glue with the main osteon orientation parallel to the normal of the stub, whereas the transverse sample was glued with the main osteon orientation parallel to the stub surface. Microtensile specimens were produced by FIB milling. Specimens were fabricated a few tens of micrometers away from the sample edge to avoid any residual damage from the cutting procedure. Two types of specimens were fabricated: multiple lamellae specimens exhibiting gauge dimensions of ~ 4 × 8 × 20 μm^3 (width, thickness, length) and single lamella specimens featuring gauge dimensions of ~ 2 × 4 × 10 μm^3 (width, thickness, length). The detailed measurements of the two geometries are illustrated in Fig. 1. Before FIB milling, samples were sputtered with a 10 nm thick gold (Au) film (Leica ACE600, Germany). A xenon (Xe) plasma-FIB (Tescan Fera, Czech Republic) operated at 30 kV was employed for the initial rough milling steps, with the intent of reducing milling time. Rectangular structures of approximatively 50 × 60 × 15 μm^3 (width, height, thickness) were fabricated at the edge of the samples using high beam currents, ranging from 1000 nA to 100 nA (Fig. S1, Supporting Information). A gallium (Ga) FIB (Tescan Lyra, Czech Republic) operated at 30 kV was employed to thin these structures to either 8 or 4 μm in thickness (Fig. S2, Supporting Information) and to mill the microtensile specimens by sequentially reducing beam currents from 10 nA to 0.2 nA (Fig. S3, Supporting Information). Backside FIB-induced redeposition was removed by an additional top milling step at the

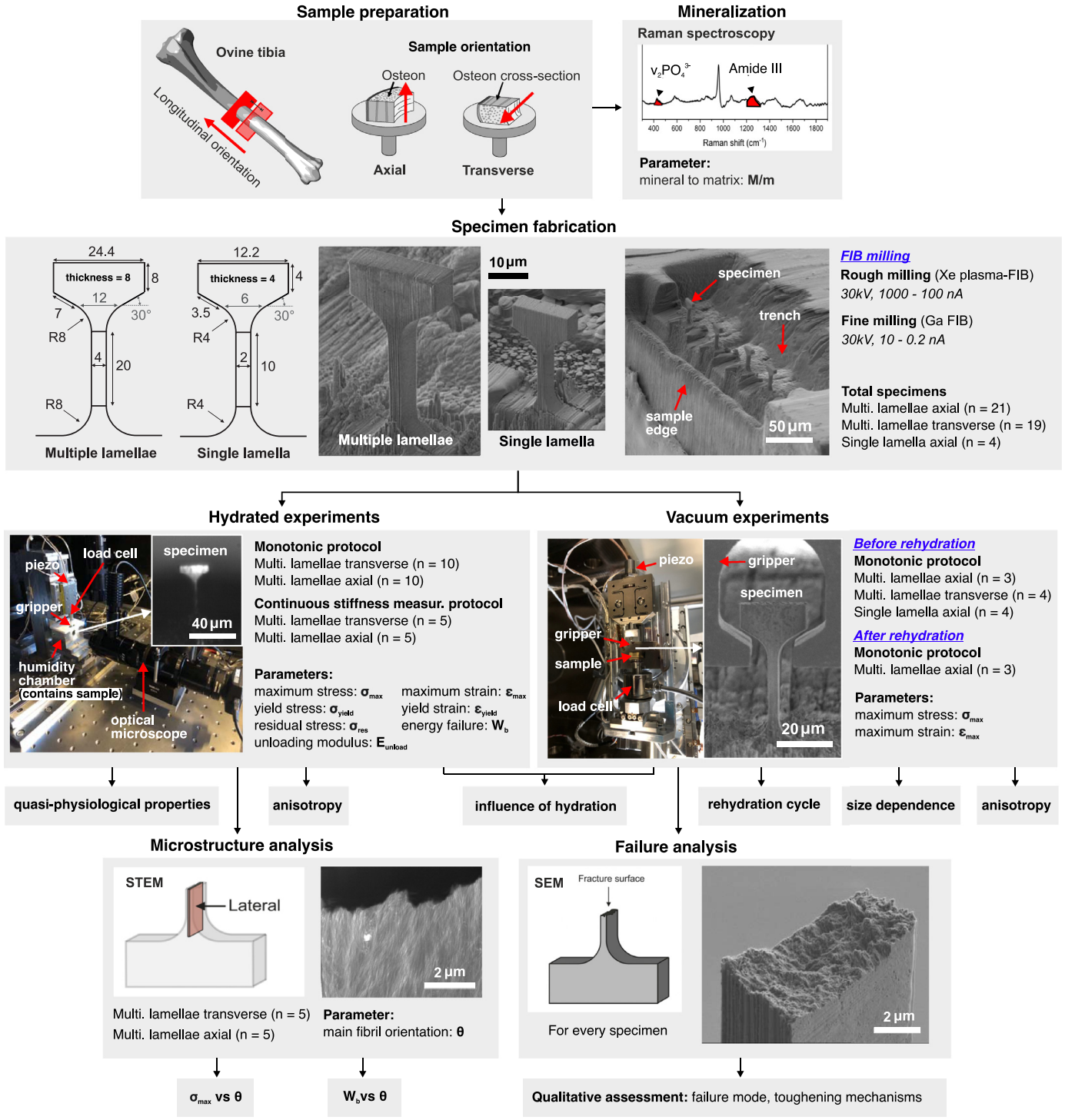

Fig. 1. Overview of the study pipeline. An ovine tibia has been cut at the diaphysis and shaped into axial and transverse samples. The degree of mineralization of each sample was analyzed with Raman spectroscopy. Successively, two types of specimen geometries were FIB milled (units are given in micrometers). Specimens were tested under both hydrated and in vacuum conditions and analyzed post-test via STEM and HR-SEM.

back of the gauge section using 0.2 nA beam current (Fig. S4, Supporting Information). A total of 48 multiple lamellae specimens (24 axial, 24 transverse) were fabricated. Furthermore, 4 single lamella specimens were fabricated in the axial direction. They constituted a control group for comparison to our previous study [46]. 8 multiple lamellae specimens (3 axial and 5 transverse) were discarded from the study as they showed osteocyte lacunae or visible microcracks on their surface.

2.2. Microtensile experiments

2.2.1. Vacuum conditions

In vacuo microtensile experiments were performed on 4 single lamella axial specimens, 6 multiple lamellae axial specimens before ($N = 3$) and after rehydration ($N = 3$, 36 h at >90% RH and air-dried for 1 week), and on 4 multiple lamellae transverse specimens after hydration. Experiments were performed using a previously

developed *in situ* microtensile setup [48] based on a commercial nanoindenter (Alemnis AG, Switzerland). The setup was placed inside an SEM (Zeiss DSM962, Germany) operating at 5 kV to collect images of the experiments and to allow gripper and specimens alignment. All the specimens tested in vacuum were monotonically loaded at a strain rate of ~ $5 \cdot 10^{-4}$ s^{-1}. Force and displacement were monitored with sampling rates of 80 Hz.

2.2.2. Hydrated conditions

Hydrated microtensile experiments were performed on 30 multiple lamellae specimens (15 axial and 15 transverse) using a custom-made setup (Hydration Microtensile Setup and Fig. S5, Supporting Information). Before mechanical testing, samples were placed in the humidity chamber at 23 °C for at least 3 h at >90% RH. Both RH and temperature inside the chamber had fluctuations smaller than 4% and 2 °C, respectively, over the whole experimental campaign (36 h). For 10 specimens of each sample type, monotonic tensile experiments were conducted at a quasi-static strain rate ~ $5 \cdot 10^{-4}$ s^{-1} (15 nm s^{-1}). For 5 axial and 5 transverse specimens, the linear loading protocol of 15 nm s^{-1} was modulated with a sinusoidal displacement of 15 nm amplitude and 0.5 Hz frequency to produce loading-unloading cycles for continuous stiffness measurement. The unloading slope was measured for each cycle to identify the changes in stiffness as a function of the applied inelastic strain. Force and displacement were monitored with sampling rates of 80 Hz.

2.2.3. Mechanical data

Load-displacement curves were converted into engineering stress-strain curves. Initially, the measured displacement was corrected for both instrument and specimen compliance to obtain the respective gauge section displacement. The compliance correction is based on the methodology described by Hajy Akbary et al. [49] and is described in the Supporting Information. The main assumptions for this methodology imply no slip at the gripper contact, a uniaxial stress state in the specimen, that plane cross-sections remain planar during deformation, and that the material behavior is linear elastic. Based on the assumption of a uniaxial stress state in the specimen gauge section, we computed engineering stress as the measured axial force divided by the initial cross-sectional area of the gauge section, whereas engineering strain was computed by dividing the corrected gauge section displacement by the initial gauge length.

Several parameters were extracted from the microtensile experiments. The yield point was defined as the intersection point of the stress-strain curve and a 0.05% offset of the loading modulus. The loading modulus was extrapolated using the highest stiffness in the elastic region through linear regression over a moving window (window size = 0.2% strain). In the absence of a yield point, the material behavior was considered brittle. When the stress-strain curve showed inelastic deformation, the total energy density to failure was calculated by integrating the area under the stress-strain curve. The ultimate point was defined as the point with the highest stress, whereas strain at failure was extrapolated as the maximum strain before complete failure. For the continuous stiffness measurement experiments, the unloading modulus evolution was extracted by linear regression on stress-strain data obtained during partial unloading cycles (Fig. S6, Supporting Information). Specifically, the central half of the data points between local maxima and minima were fitted with a linear function. The elastic modulus was calculated by averaging the unloading stiffness values before crack initiation (data included in the range above 90% of the maximum stiffness).

2.3. Imaging and microstructural characterization

SEM and scanning transmission electron microscopy (STEM) images were taken using a high-resolution (HR) SEM (Hitachi S-4800, Japan). Specimen dimensions were measured before mechanical loading at 1.5 kV and 10 µA. Secondary electron SEM images of the fracture surfaces were obtained after the microtensile experiments by using the same conditions. For both orientations, five electron transparent sections (200 nm in thickness) were prepared from the gauge section of fractured specimens using a previously established protocol [39]. STEM images of the thin sections were obtained in bright field mode, using a transmitted electron detector while operating the microscope at an acceleration voltage of 30 kV and beam current of 10 µA. Mean fibril orientation of individual sections was computed using a previously established protocol with the plug-in OrientationJ (Biomedical Imaging Group, EPFL, Switzerland) for the software ImageJ (NIH, Bethesda, Maryland, USA) [46].

2.4. Raman spectroscopy

Raman spectra were collected over ten random locations on the surface 1–2 mm away from the microtensile specimens for both axial and transverse samples. Measurements were performed in dry condition using an upright Raman microscope (Nova Spectra, NT-MDT, Russia) with a laser source with 633 nm wavelength, 11 mW power, and a 50 x objective with a numerical aperture of 0.75. Spectra were recorded at a resolution of 2 cm^{-1} with an exposure time of 60 s. Background fluorescence was removed by subtracting a 2nd order polynomial function from the raw spectra. The mineral/matrix ratio was calculated from the ratio between the integrated areas of the $v_2PO_4^{3-}$ and the amide III peaks. These peaks were chosen due to their minimal susceptibility to tissue organization and orientation effects [50]. Raman bands were fitted with double Lorentzian functions and the area of the $v_2PO_4^{3-}$ peak was integrated from 395 to 480 cm^{-1}. The area of the amide III peak was calculated by integrating from 1210 to 1325 cm^{-1}.

2.5. Statistics

All data manipulations and statistical analysis were performed using MATLAB (The MathWorks Inc, Natick, Massachusetts, USA) and R (R Foundation for Statistical Computing, Vienna, Austria). Normality of data distribution was verified by the Shapiro–Wilk test. Measurements are reported as mean ± standard deviation. Significant differences between datasets were tested using Welch's t-tests. The level of significance was set to $p \leq 0.05$.

3. Results

3.1. Microtensile experiments

Representative curves for the experiments performed *in vacuo* and under hydrated conditions are illustrated in Fig. 1. Tables 1 and 2 summarize the measured properties for vacuum and hydrated experiments, respectively.

3.1.1. Vacuum experiments

All specimens tested in vacuum showed brittle failure (Figs. S7–S9, Supporting Information). The strength of single lamella specimens in the axial orientation (thickness: 4.14 ± 0.14 µm; width: 1.83 ± 0.06 µm; gauge section length: 10.07 ± 0.13 µm) was 343 ± 38 MPa. No statistical difference ($p = 0.54$) in strength was found between the strength of ovine bone tested in this study (3.5 years old, tibia) and the younger (2 years old, tibia) ovine

Table 1
Mean and standard deviation of the properties of specimens mechanically loaded in tension under vacuum conditions. M/m: mineral to matrix ratio measured by Raman spectroscopy; Duct.: number of samples showing a significant post-yield behavior; σ_{max}: strength; ε_{max}: maximum strain.

Orientation	Length scale	M/m [a] [-]	Duct. [-]	σ_{max} [MPa]	ε_{max} [%]
Axial	Single lamella	0.91 ± 0.11	0/4	343 ± 38	2.1 ± 0.2
Axial[b]	Single lamella	0.63 ± 0.05	0/10	346 ± 54	1.8 ± 0.2
Axial	Multiple lamellae	0.91 ± 0.11	0/6	152 ± 37	1.5 ± 0.2
Transverse[b]	Single lamella	0.76 ± 0.08	0/12	130 ± 20	1.3 ± 0.3
Transverse	Multiple lamellae	0.83 ± 0.07	0/4	66 ± 13	1.1 ± 0.1

[a] ν_2PO_4/amide III ratio described by Roschger et al. [50].
[b] data from Casari et al. [46].

Table 2
Mean and standard deviation of the composition and mechanical properties of specimens loaded under tension in hydrated conditions. M/m: mineral to matrix ratio measured by Raman spectroscopy; Duct.: number of samples showing a significant post-yield behavior; σ_{max}: strength; ε_{max}: maximum strain; E_{unload}: elastic modulus; σ_{yield}: yield stress; $\varepsilon(\sigma_{yield})$: yield strain; σ_{res}: average residual stress; W_b: energy density to failure.

Orientation	M/m [a] [-]	Duct. [-]	σ_{max} [MPa]	ε_{max} [%]	E_{unload} [GPa]	σ_{yield} [MPa]	$\varepsilon(\sigma_{yield})$ [MPa]	σ_{res} [MPa]	W_b [MJ/m^3]
Axial	0.91 ± 0.11	14/15	51 ± 13	1.8 ± 0.6	15.1 ± 2.6 (N = 5)	44 ± 12	0.9 ± 0.2	14.2 ± 5.2	0.39 ± 0.19
Transverse	0.83 ± 0.07	12/15	25 ± 7	1.3 ± 0.3	5.8 ± 1.2 (N = 5)	23 ± 6	0.8 ± 0.2	3.7 ± 2.1	0.12 ± 0.06

[a] ν_2PO_4/amide III ratio described by Roschger et al. [50].

bone tested in our previous study (346 ± 54 MPa) [46]. When specimen size was increased by a factor of ~ 2 in all dimensions, a noticeable strength reduction was observed ($p < 0.01$ in both axial and transverse orientations). Multiple lamellae specimens (thickness: 8.23 ± 0.73 µm; width: 4.45 ± 0.32 µm; gage section length: 20.18 ± 0.43 µm) exhibited strength of 152 ± 37 MPa and 66 ± 13 MPa in the axial and transverse direction, respectively. The ratio between the strength of the specimens containing a single lamella and a specimen containing multiple lamellae is therefore 2.3 for the axial orientation and 2.0 for the transverse orientation (considering the transverse strength of single lamella specimens tested in vacuum to be 130 ± 20 MPa [46]). Comparison of *in vacuo* experiments performed directly after FIB fabrication (N = 3) and following a rehydration cycle at >90% (N = 3) for 36 h revealed no statistical differences for both tensile strength (p = 0.90) and strain at failure (p = 0.40).

3.1.2. Hydrated experiments

Tensile strength for multiple lamellae specimens in hydrated conditions was 51 ± 13 and 25 ± 7 MPa for axial and transverse direction, respectively. This result highlights a clear strength anisotropy ($p < 0.01$). Compared to vacuum experiments for the same specimen size, strength is reduced by a factor of 3 and 2.6 in axial and transverse directions, respectively. Experiments in hydrated conditions also showed the appearance of a significant post-yield response, as well as an increase in strain at failure. After yielding, both axial and transverse specimens showed a considerable load drop followed by a stable load plateau (87% of the cases). The average load after this initial drop was significantly higher ($p < 0.01$) for the axial specimens (14.2 ± 5.2 MPa) than for the transverse specimens (3.7 ± 2.1 MPa). In the transverse orientation, brittle failure (complete drop in stress after reaching maximum stress) was observed in 20% of the specimens. The energy density to failure was significantly higher ($p < 0.01$) for axial specimens (factor of 3.3 compared to transverse specimens). For the continuous stiffness measurement experiments, specimen stiffness initially increased until reaching a stable value of 15.1 ± 2.6 GPa (axial) and 5.8 ± 1.2 GPa (transverse) before the yield point. For three out of five axial specimens tested with the partial unloading cycling protocol, the unloading stiffness decreased after the yield point and later reached a stable value despite the increase in strain (Fig. 2c). A similar behavior was not observed in transverse specimens, in which the post-yield stiffness progressively decreased with increasing strain until failure.

3.2. Fracture surfaces

Axial specimens loaded in hydrated conditions exposed convoluted and porous fracture surfaces, featuring several protruding packs of fibrils (Fig. 3a). On the other hand, transverse fracture surfaces appeared relatively flat and smooth, with individual MCFs laying within the fracture surface (Fig. 3b). In some cases, canaliculi were observed on the fracture surface (Fig. 3b). Axial specimens tested under vacuum conditions displayed a porous structure similar to hydrated conditions but with a notably lower roughness (Fig. 3c). Transverse specimens tested in vacuum conditions exhibited similar fracture surfaces to their hydrated counterparts (Fig. 3d). No noticeable difference was observed when comparing axial fracture surfaces from specimens tested in vacuum directly after FIB fabrication or after the hydration/dehydration cycle of 36 h at >90% RH (Fig. S14, Supporting Information). No statistical difference in specimen geometry was found when comparing the measurement of width (p = 0.10) and thickness (p = 0.13) taken from the fracture surfaces (after hydration) with the measurements performed directly after specimen fabrication (before hydration).

3.3. STEM on rehydrated specimens

STEM images showed that the MCFs in axial specimens (Figs. 4a–c and S15a,b, Supporting Information) were roughly aligned with the loading direction. Conversely, in transverse specimens (Figs. 4d–f and S15c,d, Supporting Information), the MCFs were oriented perpendicular to the loading direction (except for Fig. 4f). In all the STEM images, canaliculi can be seen as white spots measuring hundreds of nanometers in diameter. In a few cases, canaliculi are found on the fracture surface, hinting to crack nucleation or crack deflection at these locations. Less dense and heterogeneous MCFs regions (dotted regions) were also observed in most STEM images. These regions most likely correspond to interlamellar interfaces. In axial specimens, when MCFs are homogeneously and densely organized, the crack propagates following a tortuous path. In the presence of interlamellar interfaces, the crack path is deviated and becomes significantly smoother (left side Fig. 4c). In transverse specimens, cracking is likely caused by

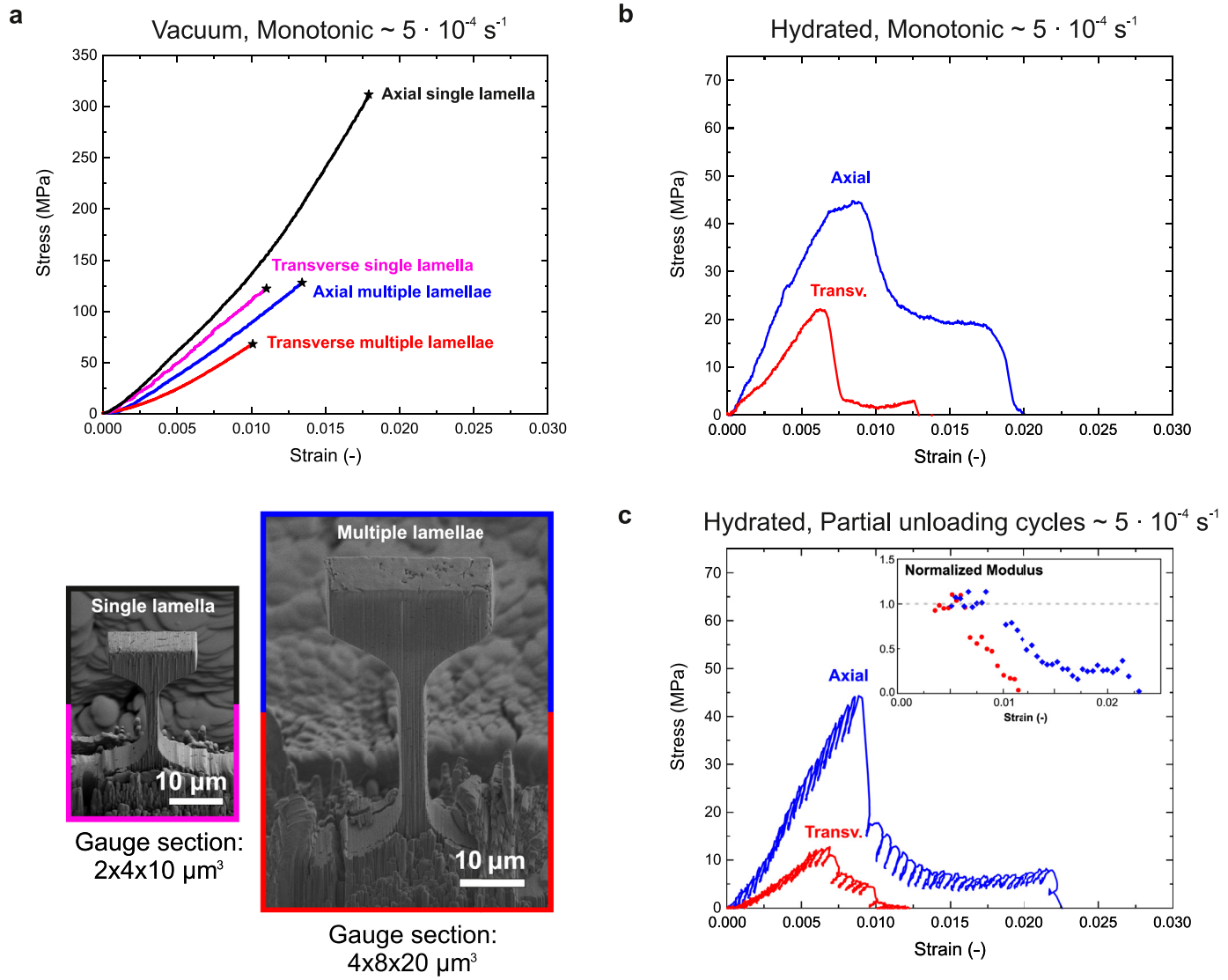

Fig. 2. Representative stress-strain curves of the *in vacuo* (a) and hydrated (b,c) microtensile experiments (notice the scale difference in the stress axis). Individual stress-strain data for each experiment can be found in the Supporting Information (Figs. S7–S11, Supporting Information). In (a), the stress-strain curve of a single lamella in transverse orientation was added from the data collected from our previous study [46]. In (c), the normalized elastic modulus obtained by the linear fit of the unloading segments of both axial (blue) and transverse (red) curves is plotted as a function of applied strain. For clarity, the initial increase in modulus has been removed (but can be seen in Figs. S12 and S13, Supporting Information). (For interpretation of the references to color in this figure legend, the reader is referred to the web version of this article.)

the critical orientation of these weak interfaces, which is perpendicular to the loading direction.

From ten STEM images (Figs. 4 and S15, Supporting Information), the main fibril orientation was characterized using the plug-in OrientationJ for ImageJ (NIH, Bethesda, Maryland, USA). For the rehydrated specimens, strength as a function of the main MCFs orientation is illustrated in Fig. 5a. This trend was described using the Tsai-Hill failure criterion as it could be directly applied to the data measured in this study. The failure criterion is defined by:

$$\left(\frac{\sigma\cos^2(\theta)}{T_{11}}\right)^2 - \left(\frac{\sigma\cos(\theta)\sin(\theta)}{T_{11}}\right)^2 + \left(\frac{\sigma\sin^2(\theta)}{T_{22}}\right)^2 + \left(\frac{\sigma\cos(\theta)\sin(\theta)}{S_{12}}\right)^2 = 1 \quad (1)$$

Where T_{11} and T_{22} are the measured tensile strengths in the axial ($\theta = 0°$) and transverse ($\theta = 90°$) directions, respectively. S_{12} represents the shear strength of the composite and it is regarded as a fitting parameter (sum-of-squares optimization). The model was described using the strength data summarized in Table 2 and the fitting parameter S12 = 18.2 MPa (shear strength). The total energy density to failure with respect to MCF main orientation showed a marked dependency for MCF orientations <25 (Fig. 5b).

4. Discussion

4.1. Single lamella microtensile properties

Single lamella specimens were tested under vacuum conditions as a way to compare tissue properties among biopsies from the same species. Tensile strength (343 ± 38 MPa), strain at failure (2.1 ± 0.2%), and brittle failure were comparable to our previous work for similar specimens sizes, even though the samples of this study showed a higher mineral to matrix ratio (0.91 ± 0.11 vs. 0.63 ± 0.05, $p<0.01$) [46]. The difference in the mineralization content can be related to the difference in age between the biopsies (3.5 and 2 years old). However, the age difference was not enough

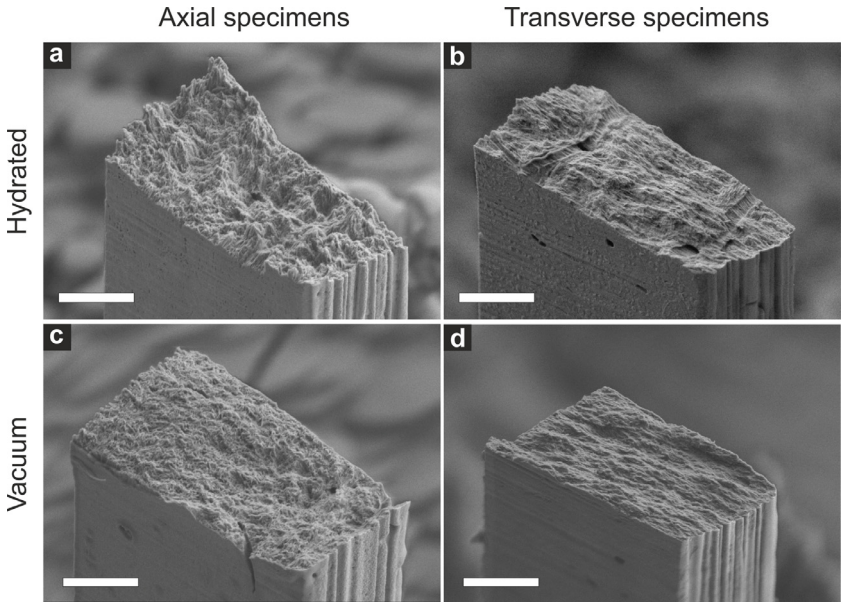

Fig. 3. SEM images of fractured axial and transverse specimens in hydrated (a,b) and vacuum (c,d) conditions. Scale bars represent 2 µm.

to reveal any significant change in the mechanical properties between the biopsies. Despite this, these results support the notion that at the lamellar level the mineral phase is mostly responsible for the compressive strength in bone, while the organic phase (collagen, non-collagenous proteins) most likely regulates bone's tensile strength properties [51–53].

4.2. Specimen size effect

To investigate the influence of specimen size, *in vacuo* microtensile experiments were also performed on larger specimens containing more than one lamella. As for single lamella specimens, all multiple lamellae specimens loaded *in vacuo* showed brittle failure (Figs. 2, S8 and S9, Supporting Information). However, by increasing specimen size by a factor of 2 in all dimensions, a noticeable strength reduction was observed. Multiple lamellae specimens failed at significantly lower stress of 152 ± 37 MPa and 66 ± 13 MPa in axial and transverse orientation, respectively. Additionally, the change in geometry resulted in a ~15% decrease in the strain at failure in both orientations. These results may be rationalized with the stochastic nature of flaws in bone and a less homogeneous orientation distribution of the microarchitectural features, i.e., MCF orientation, canalicular and interlamellar interface orientation, in larger specimens. This is supported by the larger experimental scatter in the strength obtained for multiple lamellae specimens (20–24% standard deviation) compared to single lamella specimens (10–15% standard deviation). When testing larger volumes, not only more weak interfaces are included, but the probability of loading one of these interfaces in a critical orientation also increases, leading to a decrease in the average strength of the cohort of specimens. The same principle is valid for lacunocanalicular porosity. By increasing the specimen volume, there is a higher probability of including canaliculi running perpendicularly to the loading direction. For an isotropic material, a similar defect gives rise to a stress concentration with a stress peak 3 times higher than the average stress in the gauge section [54]. If such a defect interacts closely with an interface, strength is heavily affected. The likelihood of this adverse coaction increases with specimen size. This could also explain why the Tsai-Hill model applied to multiple hydrated lamellae data yielded a shear strength of 18.2 MPa. Compared to the extrafibrillar matrix shear strength measured by Gupta et al. of 60–80 MPa [55], our shear strength value is a factor 3–4 lower. This may be justified by the influence of the canalicular porosity and interlamellar interfaces on our microscale samples, which lead to significant stress concentrations ($K = 3$ for canaliculi oriented perpendicular to the loading direction for an isotropic material). Moreover, a broader distribution in MCF orientation is also expected as the dimensions of the rehydrated specimens become comparable to the typical size of bone lamellae (3–7 µm). Variation of MCF orientation throughout the gauge section (Fig. S16, Supporting Information) may reduce the strength of axial specimens even further, as regions with transversally oriented MCFs facilitate early crack nucleation. In transverse specimens, the average MCF orientation distribution seems less relevant, as the crack most likely nucleates at the weakest spot, often an internal interface.

4.3. Influence of rehydration

Compared to vacuum experiments for multiple lamellae specimens, hydrated experiments showed lower strength and lower elastic modulus. Furthermore, the presence of water also led to the emergence of a significant post-yield ductility (Fig. 2). The reduction of mechanical properties and the appearance of inelastic deformation upon tissue rehydration have been observed in several studies, including tensile tests at the mesoscale (hundreds of micrometers) [47], nanoindentation [56], and micropillar compression [39]. In our work, multiple lamellae axial and transverse specimens exhibited a strength of 51 ± 13 MPa and 25 ± 7 MPa, respectively, which corresponds to a strength reduction by a factor between 2.6 and 3 compared to vacuum experiments (Fig. 6). A similar decrease in strength upon tissue rehydration was found for micropillar compression experiments (diameter ~ 5 µm, height ~ 10 µm) on ovine lamellar bone performed in similar experimental conditions [39]. The tensile strength and the material behavior of multiple lamellae specimens in hydrated conditions reported in this work are comparable with the multiscale model proposed by Wang and Ural [57], in which they describe the mechanical response of multiple MCF arrays (lamellae) connected through zero-thickness cohesive elements (interfaces).

It is important to mention that the measured properties in this work do not represent the macroscale properties of bone but they

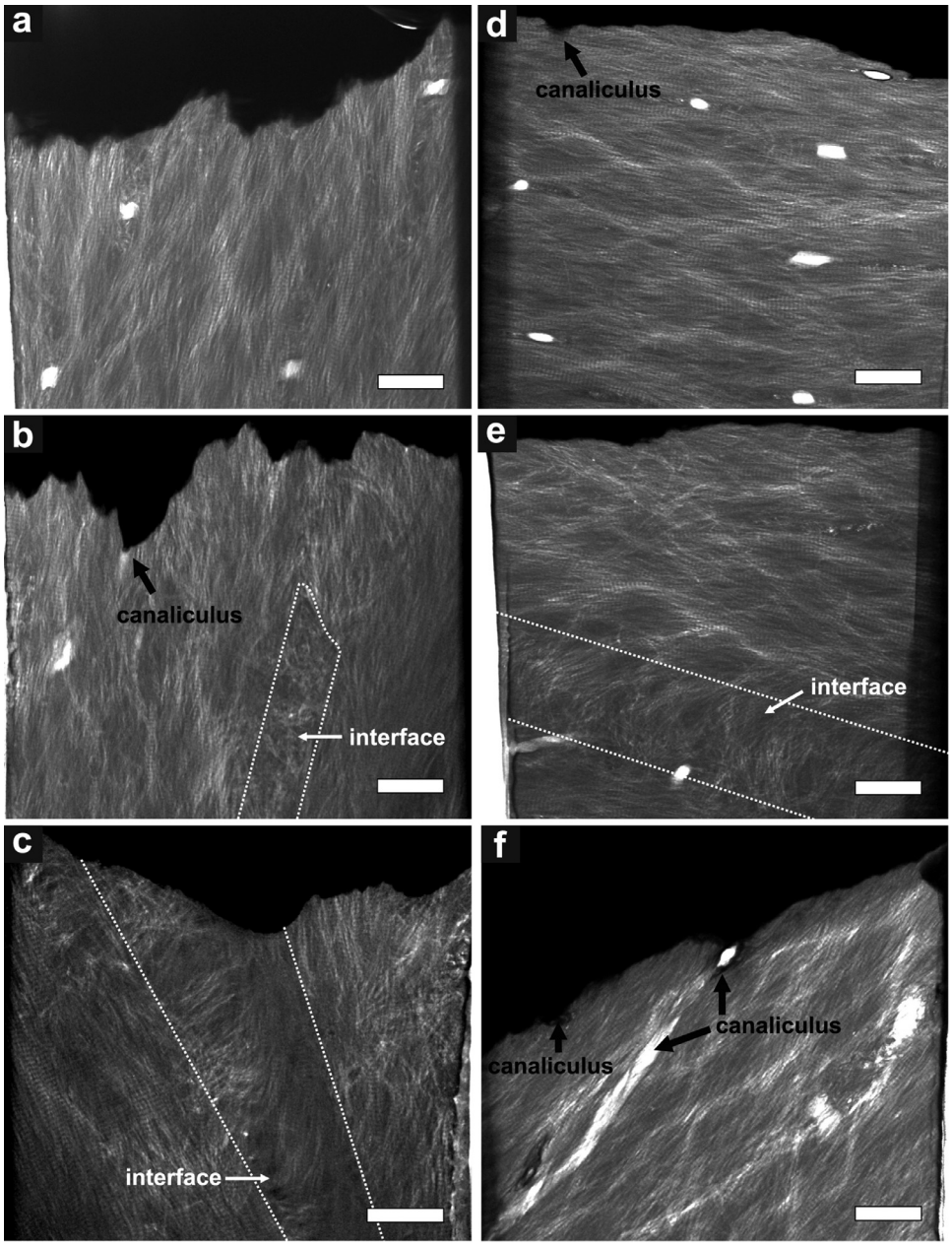

Fig. 4. STEM images of 200 nm thick sections of axial (a–c) and transverse (d–f) specimens tested in hydrated conditions. The STEM lamellae were collected from the lower part of the fractured gauge sections (see Fig. 1). The left side of the section represents the front of the specimens, whereas the right side represents the back of the specimens. In (b)–(e), disordered areas/interfaces are delimited and highlighted by white dashed lines. Black arrows indicate canaliculi lying on the fracture surface. In (f), a canaliculus is seen propagating to the surface. Scale bars represent 1 μm.

are associated with a length scale confined to a few lamellar units. That is, for the first time we report the anisotropic stress and energy needed to nucleate a single crack in crack-free hydrated lamellae (Table 2). At the macroscale, this observation would not be possible since a millimeter-sized sample already contains several microcracks generated by fatigue loading during daily activity. Furthermore, the sensitivity of the macroscale experiments is not high enough to reliably capture the nucleation of a single crack of non-critical dimension, as it integrates over a large, heterogeneous volume of interest and the definition of yield stress that is usually employed is based on the accumulation of inelastic strains and therefore the initiation of a large number of sub-critical cracks [45]. Finally, it is critical to note that the stress to initiate a microscopic crack in bone can be significantly lower than bone's macroscale strength. The presence of several extrinsic toughening mechanisms acting at the length scale of tens to hundreds of micrometers makes it significantly easier to nucleate a crack compared to propagating a crack up to the macroscopic critical crack length [58]. The latter can be explained by the increasing *R*-curve behavior of bone: as long as the length of the crack is sub-critical, the fracture resistance of bone increases with crack length, thus allowing stable crack growth. When a crack reaches a critical length, fracture becomes catastrophic. In bone, this value is in the order of 300–400 μm [58]. This is in line with the formation of microdamage upon overloading in bone that consists of the nucleation of myriads of sub-critical cracks that enables the accommodation of inelastic strains at the macroscale without catastrophic failure [45]. Since our experiments were confined to a few

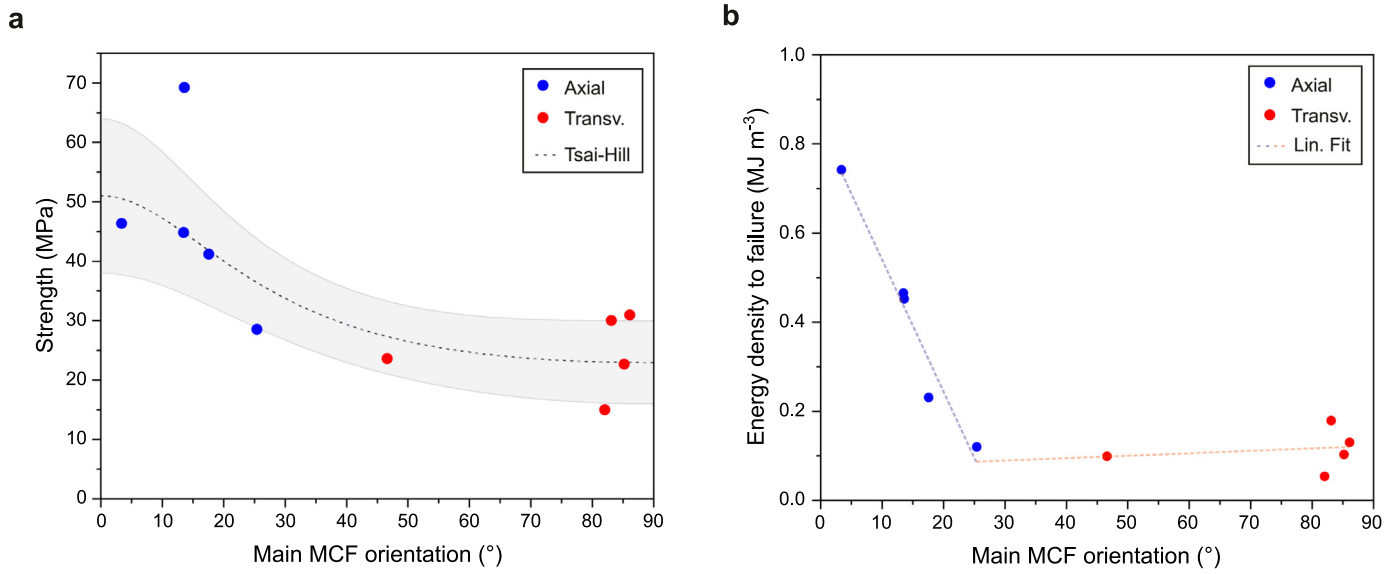

Fig. 5. Tensile strength (a) and total energy density to failure (b) of hydrated specimens as a function of MCF main orientation measured via STEM analysis. In (a), the Tsai-Hill model was incorporated using the measured anisotropic strength reported in Table 2. The gray area was constructed using standard deviation values in Table 2 to fit the model. In (b), linear regressions for both axial and transverse specimens are illustrated with colored dashed lines.

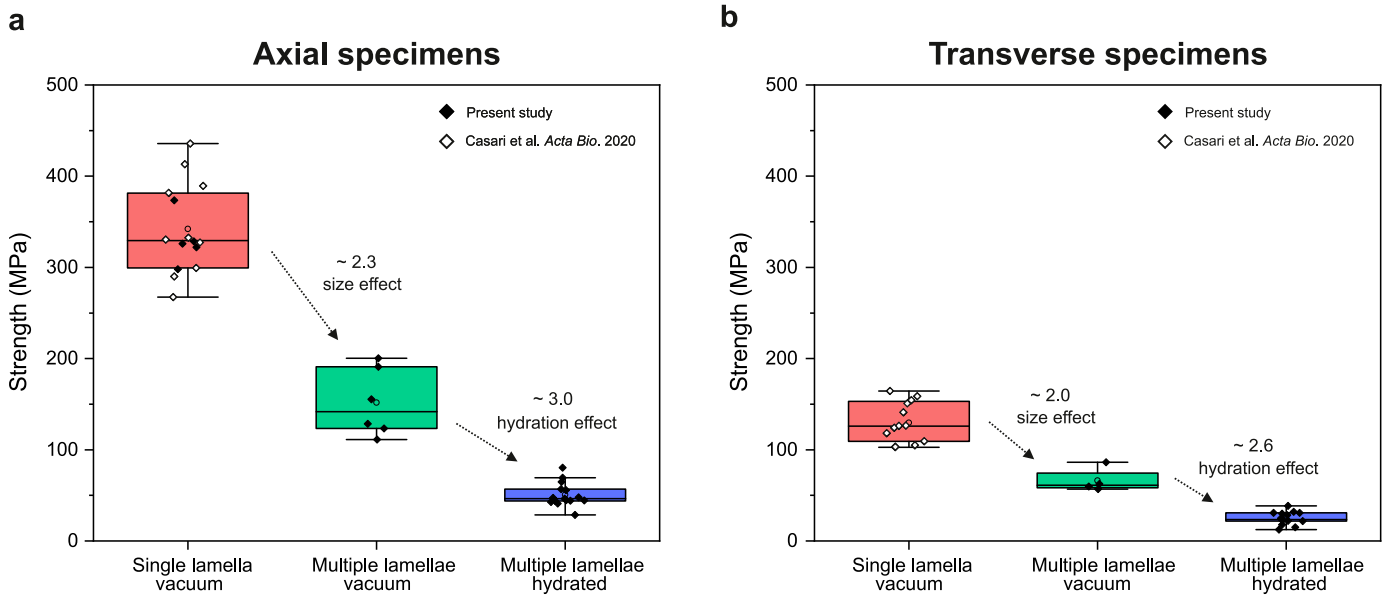

Fig. 6. Specimens size effect and hydration effect on the microtensile strength of lamellar bone on axial (a) and transverse (b) orientation. For single lamella specimens, the specimen strength (130 ± 20 MPa) collected in a previous study was included in the plots (in white) [46]. Boxplots were created using the standard boxplot chart in OriginLab (OriginLab Corporation, Northampton, MA, USA). The box length is the interquartile range. A line across the box indicates the median. Whiskers length coefficient is set to 1.5.

lamellae, we are focusing our observations on a length scale at which a single crack can appear, but it cannot be effectively countered by any important extrinsic mechanism found at higher length scales, such as uncracked ligament bridging or crack deflection at the cement lines. Therefore, our results are related to crack initiation rather than to crack propagation. In macroscale specimens multiple sub-critical cracks may accumulate before failure [37]. In our experiment, when a single crack is nucleated it is then propagated through the whole specimen leading to a catastrophic fracture event.

Compared to nanoindentation and micropillar experiments on hydrated ovine bone [39], the elastic modulus measured in this work is relatively low, especially in the transverse orientation (5.8 ± 1.2 GPa). While a reduction in elastic modulus upon tissue rehydration is expected, this value is likely affected by surface swelling artifacts (see Limitations).

Finally, despite water induces surface swelling artifacts, hydrating and successively drying the specimens did not significantly affect their mechanical properties, as well as their deformation mechanisms (Absence of Swelling Related Damage, Supporting Information).

4.4. Microstructure

The anisotropic strength of bone was successfully described as a function of mean fibril orientation using the Tsai-Hill fail-

ure criterion for uniaxial fiber composites (Fig. 5a). MCF orientation has shown to play an essential role in defining lamellar bone strength. Nevertheless, strength is likely influenced by other factors such as the presence and orientation of weak interfaces and pores. In hydrated conditions, the strength anisotropy ratio between multiple lamellae axial and transverse specimens was slightly reduced from 2.3:1 (vacuum) to 2:1 (rehydrated). By increasing the size of the specimen, MCF orientation becomes less influential than in single lamella specimens. The STEM images suggest that bone retains its anisotropic nature over several length scales, allowing for a multiscale preferential (and non-critical) crack propagation. This is the result of a recurring structure within bone's structural elements: a strong, stiff, and axially oriented element surrounded by a weak interface. At the macroscale, osteons deviate cracks in the longitudinal orientation through cement sheaths [31,32]. At the microscale, lamellae are separated by weak interlamellar interfaces, whereas at an even lower scale, individual MCFs are interconnected by a weak organic interface [25,26].

4.5. Toughening mechanisms

When comparing fracture surfaces, it is clear that the experiments performed on hydrated specimens resulted in rougher fracture surfaces compared to *in vacuo* tests, especially for axial specimens, where the difference was striking (Fig. 3a and c). The tortuous crack paths featuring several protruding packs of fibrils in axial fracture surfaces are reminiscent of macroscopic fracture surfaces [17]. It suggests the presence of crack-shielding mechanisms at these length scales, such as crack deviation and fibril bridging. As the fibrils are oriented perpendicular to the crack path, they can resist complete failure of the nanocomposite through MCF bridging. STEM images showed evidence of crack kinking due to the presence of defects such as porosity or interfaces (Fig. 4). In 60% of the cases, after an initial decrease in stiffness related to the nucleation of a crack, the post-yield stress and stiffness both reached a plateau despite an increase in strain. Once the crack has stabilized, the remaining MCFs are able to resist failure by inherent plastic deformation via intermolecular slip at the mineral-collagen interface [20]. The sharp increase in energy density to failure in specimens exhibiting main MCF orientation $<25°$ (Fig. 5b) indicates the range for which fibril bridging is efficient. Based on the average value of the post-yield residual stress, we can estimate how many MCFs are resisting failure through fibril bridging. Assuming fibril diameter to be 92 nm, hexagonal MCF packing with an interfibrillar distance of 2 nm, fibril strength of 118.7 MPa [59], and that the plateau stress in axial specimens (14.2 $\pm$ 5.2 MPa) is generated by MCF bridging only, one finds that the minimum number of MCFs resisting the fracture is on the order of 600 $\pm$ 200. Based on the same architectural assumptions, the total number of MCFs in a specimen featuring a gauge section of 4.45 $\times$ 8.23 μm^2 (average) includes approximately 5000 MCFs. About 12% of the fibrils are resisting fracture following initial crack initiation, which is in line with the average normalized residual stiffness (16 $\pm$ 4%). On the other hand, in transverse specimens, crack nucleation occurs at much lower loads. The post-yield stiffness decreases progressively until failure despite the unfavorable MCF orientation (Figs. 2 and S13, Supporting Information), suggesting the presence of a crack-tip plasticity mechanism. This result hints at an intrinsic toughening mechanism located at the lamellar interfaces. The mechanism is most likely mediated by the high number of NCPs in the interlamellar interfaces [60], enabling hidden length and sacrificial bond mechanisms [24–26]. Factors such as age and disease could influence how these interfaces behave mechanically, thus leading to brittle failure.

4.6. Limitations

4.6.1. Surface effects

The experiments were performed in humid conditions only (no saline solution). Although physiological conditions are commonly replicated using saline solution, the presence of salts has shown to have almost no effects on collagen fibrils mechanics [62]. A more important limitation is that lamellae were not enclosed by their natural surroundings. Because of this, fibril swelling is expected upon hydration, especially at the surface of the specimens [61]. Surface bulging lowers the contact stiffness between the gripper and the specimen and could explain the low elastic modulus measured in this study [42]. It is unlikely that the low modulus could be related to the glue used to attach the samples to the SEM stubs. The glue is water resistant and it is stressed with less than 1 kPa. Andriotis et al. [62]. observed radial swelling up to a factor 2 in non-mineralized collagen fibrils, which led to a 24-fold reduction in radial stiffness. In transverse specimens, this effect is potentially strong since the MCFs are oriented perpendicularly to the loading direction. In axial specimens, the swelling artifact is less influential since the fibril are primarily oriented parallel to the loading direction. However, since all specimens feature 30° contact flanges, a noticeable stiffness decrease is also expected in axial specimens. This is in line with our observations.

4.6.2. Micromechanics

A well-known restriction in micromechanics is the limited number of samples produced due to the time-consuming preparation process. To overcome this limitation, experiments were conducted on ovine bone. The latter has a similar structure to human bone at the nanoscale but exhibits a more homogenous MCF organization and mineralization at the microscale [39]. This leads to significantly lower experimental scatter and allowed us to contribute to the fundamental understanding of the structure-property relationships and nanoscale behavior of bone structural units. The microtensile properties of ovine bone tested *in vacuo* were found to be statistically identical to a previous study [46], showing a promising consistency in mechanical properties at the microscale. Nevertheless, this remains speculation and it should be investigated with further studies. Assuming this, the data collected in this study may be used to describe the behavior of an individual lamellar ply. By knowing the mechanical properties of this building block, it is possible to construct the behavior of more complex laminates using computational analysis. For micropillar compression, healthy human bone revealed an axial yield strength of 350 $\pm$ 97 MPa [43]. Assuming that in human bone the MCFs are organized in a plywood-like structure, the yield strength of human bone matches well the average compressive yield strengths previously measured for ovine bone (490 $\pm$ 100 MPa for axial pillars and transverse 300 $\pm$ 0.20 GPa for transverse pillars [38]).

4.6.3. FIB milling

FIB milling is known to introduce artifacts such as surface damage and redeposition. Several steps were performed to reduce both effects to a negligible amount. Monte Carlo simulations and STEM observations suggested that FIB damage was constrained in a surface layer lower than 25 nm [38]. On the other hand, FIB milling requires vacuum conditions, which might affect the tissue microstructure. The results in this work indicated that the mechanical properties measured before and after hydration showed no statistical difference. Nevertheless, there is no way to assess the changes for the first drying cycle. A possible solution to avoid vacuum could rely on ultrafast laser ablation for specimen preparation at the expense of milling resolution [63].

4.6.4. Strain measurement

The specimen strain is calculated indirectly through a compliance correction. This methodology assumes no slip at the gripper contact, a uniaxial stress state in the specimen, that plane cross-sections remain planar during deformation, and linear elastic material behavior. Since these assumptions might not be met at all locations in the specimen, one should expect some uncertainty for the strain values. The microtensile methodology previously showed an uncertainty of 5–15% on the total strain measured [48] and was shown to allow measuring the modulus during partial unloading cycles with an error <5%. This level of accuracy is comparable to other standard micromechanical testing techniques such as micropillar compression [64]. Despite this, the compliance correction is a practical alternative to digital image correlation for the measurement of strain, especially when an accurate observation of the sample surface is impossible i.e., when performing experiments in humid conditions (due to the limited resolution of the optical setup).

5. Conclusions

In this work, the anisotropic microtensile properties of bone were investigated at the length scale of a few lamellar units in both dry and hydrated conditions. The main findings were:

- A clear anisotropy in tensile properties was found: axial specimens with MCF oriented parallel to the loading direction were stronger, stiffer, and tougher than transverse specimens. Energy dissipation was also highly dependent on local MCF orientation. In axial specimens, fibril bridging and crack kinking resulted in tortuous crack paths resembling macroscopic fracture surfaces. In transverse specimens, a smoother fracture surface and a continuous crack growth up to failure were observed, suggesting a possible intrinsic mechanism mediated by NCP-rich interfaces.
- A specimen size effect was identified: when specimen size was increased from a single lamellar unit to a few lamellar units, a significant decrease in strength was observed. This is rationalized by the higher probability of finding flaws (canaliculus, interlamellar interface) in a critical orientation when assessing larger volumes.
- Hydration was shown to strongly affect mechanical behavior in tension: comparison of experiments in dry and hydrated states revealed the critical role of water in the nanocomposite. Strength was reduced by 60–65% upon rehydration in both directions. At the same time, we observed water-activated extrinsic and intrinsic toughening mechanisms leading to a significant post-yield ductility on the lamellar level.

For the first time, we report the nucleation of a single crack in hydrated bone lamella under well-controlled uniaxial tensile loading, highlighting the role of interfaces, defects, and the ratio of defect to specimen size on the apparent properties of lamellar bone. These results fill a significant knowledge gap in the literature and can be used in the future to develop multiscale models enabling improved clinical management of disease-related bone fractures.

Author contributions

The initial planning of the study was done by D.C., J.S., J.M., and P.Z. Microtensile specimens were fabricated by D.C. Mechanical tests and SEM/STEM imaging were performed by D.C. Raman spectroscopy was performed by T. K. Data analysis and interpretation was performed by D.C. in cooperation with J.S. The manuscript was written by D.C. with contributions from all the authors.

Declaration of Competing Interest

The authors declare that they have no known competing financial interests or personal relationships that could have appeared to influence the work reported in this paper.

Acknowledgments

This study was funded by the Swiss National Science Foundation (SNSF) Grant No. 165510 (DC) and Ambizione grant no. 174192 (JS). TK acknowledges funding through SFA PHRT iDoc grant 2017–304. The authors acknowledge the Scientific Center for Optical and Electron Microscopy ScopeM of the Swiss Federal Institute of Technology ETH Zürich for providing access to their facilities. The authors would like to thank Dr. J. Reuteler for his assistance during plasma-FIB milling.

Supplementary materials

Supplementary material associated with this article can be found, in the online version, at doi:10.1016/j.actbio.2021.06.032.

References

[1] N. Harvey, E. Dennison, C. Cooper, Osteoporosis: impact on health and economics, Nat. Rev. Rheumatol. 6 (2) (2010) 99–105.
[2] J.Y. Rho, L. Kuhn-Spearing, P. Zioupos, Mechanical properties and the hierarchical structure of bone, Med. Eng. Phys. 20 (2) (1998) 92–102.
[3] P. Fratzl, H.S. Gupta, E.P. Paschalis, P. Roschger, Structure and mechanical quality of the collagen-mineral nano-composite in bone, J. Mater. Chem. 14 (14) (2004) 2115–2123.
[4] D.H. Pahr, P.K. Zysset, Finite element-based mechanical assessment of bone quality on the basis of in vivo images, Curr. Osteoporos. Rep. 14 (6) (2016) 374–385.
[5] M.A. Rubin, I. Jasiuk, J. Taylor, J. Rubin, T. Ganey, R.P. Apkarian, TEM analysis of the nanostructure of normal and osteoporotic human trabecular bone, Bone 33 (3) (2003) 270–282.
[6] A. Gautieri, S. Vesentini, A. Redaelli, M.J. Buehler, Hierarchical structure and nanomechanics of collagen microfibrils from the atomistic scale up, Nano Lett. 11 (2) (2011) 757–766.
[7] N. Reznikov, M. Bilton, L. Lari, M.M. Stevens, R. Kröger, Fractal-like hierarchical organization of bone begins at the nanoscale, Science 360 (2018) 1–10.
[8] P. Fratzl, R. Weinkamer, Nature's hierarchical materials, Prog. Mater. Sci. 52 (8) (2007) 1263–1334.
[9] S. Weiner, H.D. Wagner, The material bone: structure-mechanical function relations, Annu. Rev. Mater. Sci. 28 (1) (1998) 271–298.
[10] P. Varga, A. Pacureanu, M. Langer, H. Suhonen, B. Hesse, Q. Grimal, P. Cloetens, K. Raum, F. Peyrin, Investigation of the three-dimensional orientation of mineralized collagen fibrils in human lamellar bone using synchrotron X-ray phase nano-tomography, Acta Biomater. 9 (9) (2013) 8118–8127.
[11] S. Schrof, P. Varga, L. Galvis, K. Raum, A. Masic, 3D Raman mapping of the collagen fibril orientation in human osteonal lamellae, J. Struct. Biol. 187 (3) (2014) 266–275.
[12] M.M. Giraud-Guille, Twisted plywood architecture of collagen fibrils in human compact bone osteons, Calcif. Tissue Int. 42 (3) (1988) 167–180.
[13] J. Heřt, P. Fiala, M. Petrtýl, Osteon orientation of the diaphysis of the long bones in man, Bone 15 (3) (1994) 269–277.
[14] L.F. Bonewald, The amazing osteocyte, J. Bone Miner. Res. 26 (2) (2011) 229–238.
[15] F. Repp, P. Kollmannsberger, A. Roschger, A. Berzlanovich, G.M. Gruber, P. Roschger, W. Wagermaier, R. Weinkamer, Coalignment of osteocyte canaliculi and collagen fibers in human osteonal bone, J. Struct. Biol. 199 (3) (2017) 177–186.
[16] R.O. Ritchie, M.J. Buehler, P. Hansma, Plasticity and toughness in bone, Phys. Today 62 (6) (2009) 41–47.
[17] M.E. Launey, M.J. Buehler, R.O. Ritchie, On the mechanistic origins of toughness in bone, Annu. Rev. Mater. Res. 40 (1) (2010) 25–53.
[18] E.A. Zimmermann, R.O. Ritchie, Bone as a structural material, Adv. Healthc. Mater. 4 (9) (2015) 1287–1304.
[19] A. Gautieri, M.J. Buehler, A. Redaelli, Deformation rate controls elasticity and unfolding pathway of single tropocollagen molecules, J. Mech. Behav. Biomed. Mater. 2 (2) (2009) 130–137.
[20] M.J. Buehler, Molecular nanomechanics of nascent bone: fibrillar toughening by mineralization, Nanotechnology 18 (29) (2007) 295102.
[21] B. Depalle, Z. Qin, S.J. Shefelbine, M.J. Buehler, Influence of cross-link structure, density and mechanical properties in the mesoscale deformation mechanisms of collagen fibrils, J. Mech. Behav. Biomed. Mater. 52 (2015) 1–13.
[22] F. Hang, H.S. Gupta, A.H. Barber, Nanointerfacial strength between non-collagenous protein and collagen fibrils in antler bone, J. R. Soc. Interface 11 (92) (2014) 20130993.

[23] H.S. Gupta, J. Seto, W. Wagermaier, P. Zaslansky, P. Boesecke, P. Fratzl, Cooperative deformation of mineral and collagen in bone at the nanoscale, Proc. Natl. Acad. Sci. U. S. A. 103 (47) (2006) 17741–17746.
[24] J.B. Thompson, J.H. Kindt, B. Drake, H.G. Hansma, D.E. Morse, P.K. Hansma, Bone indentation recovery time correlates with bond reforming time, Nature 414 (6865) (2001) 773–776.
[25] G.E. Fantner, T. Hassenkam, J.H. Kindt, J.C. Weaver, H. Birkedal, L. Pechenik, J.A. Cutroni, G.A.G. Cidade, G.D. Stucky, D.E. Morse, P.K. Hansma, Sacrificial bonds and hidden length dissipate energy as mineralized fibrils separate during bone fracture, Nat. Mater. 4 (2005) 612–616.
[26] P.K. Hansma, G.E. Fantner, J.H. Kindt, P.J. Thurner, G. Schitter, P.J. Turner, S.F. Udwin, M.M. Finch, Sacrificial bonds in the interfibrillar matrix of bone, J. Musculoskelet. Neuronal Interact. 5 (4) (2005) 313–315.
[27] D. Vashishth, K.E. Tanner, W. Bonfield, Experimental validation of a microcracking-based toughening mechanism for cortical bone, J. Biomech. 36 (1) (2003) 121–124.
[28] P. Zioupos, J.D. Currey, The extent of microcracking and the morphology of microcracks in damaged bone, J. Mater. Sci. 29 (4) (1994) 978–986.
[29] D. Vashishth, J.C. Behiri, W. Bonfield, Crack growth resistance in cortical bone: concept of microcrack toughening, J. Biomech. 30 (8) (1997) 763–769.
[30] G.P. Parsamian, T.L. Norman, Diffuse damage accumulation in the fracture process zone of human cortical bone specimens and its influence on fracture toughness, J. Mater. Sci. Mater. Med. 12 (9) (2001) 779–783.
[31] K.J. Koester, J.W. Ager, R.O. Ritchie, The true toughness of human cortical bone measured with realistically short cracks, Nat. Mater. 7 (8) (2008) 672–677.
[32] H. Peterlik, P. Roschger, K. Klaushofer, P. Fratzl, From brittle to ductile fracture of bone, Nat. Mater. 5 (1) (2006) 52–55.
[33] R.K. Nalla, J.H. Kinney, R.O. Ritchie, Mechanistic fracture criteria for the failure of human cortical bone, Nat. Mater. 2 (3) (2003) 164–168.
[34] F. Barthelat, Z. Yin, M.J. Buehler, Structure and mechanics of interfaces in biological materials, Nat. Rev. Mater. 1 (2016) 1–16.
[35] K. Tai, M. Dao, S. Suresh, A. Palazoglu, C. Ortiz, Nanoscale heterogeneity promotes energy dissipation in bone, Nat. Mater. 6 (6) (2007) 454–462.
[36] B. Ji, H. Gao, Mechanical principles of biological nanocomposites, Annu. Rev. Mater. Res. 40 (1) (2010) 77–100.
[37] P. Fratzl, Bone fracture: when the cracks begin to show, Nat. Mater. 7 (8) (2008) 610–612.
[38] J. Schwiedrzik, R. Raghavan, A. Bürki, V. Lenader, U. Wolfram, J. Michler, P. Zysset, *In situ* micropillar compression reveals superior strength and ductility but an absence of damage in lamellar bone, Nat. Mater. 13 (7) (2014) 740–747.
[39] J. Schwiedrzik, A. Taylor, D. Casari, U. Wolfram, P. Zysset, J. Michler, Nanoscale deformation mechanisms and yield properties of hydrated bone extracellular matrix, Acta Biomater. 60 (2017) 302–314.
[40] K.W. Luczynski, A. Steiger-Thirsfeld, J. Bernardi, J. Eberhardsteiner, C. Hellmich, Extracellular bone matrix exhibits hardening elastoplasticity and more than double cortical strength: evidence from homogeneous compression of non-tapered single micron-sized pillars welded to a rigid substrate, J. Mech. Behav. Biomed. Mater. 52 (2015) 51–62.
[41] O.A. Tertuliano, J.R. Greer, The nanocomposite nature of bone drives its strength and damage resistance, Nat. Mater. 15 (11) (2016) 1195–1202.
[42] T. Kochetkova, C. Peruzzi, O. Braun, J. Overbeck, A.K. Maurya, A. Neels, M. Calame, J. Michler, P. Zysset, J. Schwiedrzik, Combining polarized Raman spectroscopy and micropillar compression to study microscale structure-property relationships in mineralized tissues, Acta Biomater. 119 (2021) 390–404.
[43] M. Indermaur, D. Casari, T. Kochetkova, C. Peruzzi, E. Zimmermann, F. Rauch, B. Willie, J. Michler, J. Schwiedrzik, P. Zysset, Compressive strength of iliac bone ECM is not reduced in osteogenesis imperfecta and increases with mineralization, J. Bone Miner. Res. (2021) 1–12, doi:10.1002/jbmr.4286.
[44] U. Wolfram, J.J. Schwiedrzik, M.J. Mirzaali, A. Bürki, P. Varga, C. Olivier, F. Peyrin, P.K. Zysset, Characterizing microcrack orientation distribution functions in osteonal bone samples, J. Microsc. 264 (3) (2016) 268–281.
[45] M.J. Mirzaali, A. Bürki, J. Schwiedrzik, P.K. Zysset, U. Wolfram, Continuum damage interactions between tension and compression in osteonal bone, J. Mech. Behav. Biomed. Mater. 49 (2015) 355–369.
[46] D. Casari, J. Michler, P. Zysset, J. Schwiedrzik, Microtensile properties and failure mechanisms of cortical bone at the lamellar level, Acta Biomater. 120 (2021) 135–145.
[47] J. Seto, H.S. Gupta, P. Zaslansky, H.D. Wagner, P. Fratzl, Tough lessons from bone: extreme mechanical anisotropy at the mesoscale, Adv. Funct. Mater. 18 (13) (2008) 1905–1911.
[48] D. Casari, L. Pethö, P. Schürch, X. Maeder, L. Philippe, J. Michler, P. Zysset, J. Schwiedrzik, A self-aligning microtensile setup: application to single-crystal GaAs microscale tension–compression asymmetry, J. Mater. Res. 34 (14) (2019) 2517–2534.
[49] F. Hajy Akbary, M.J. Santofimia, J. Sietsma, Elastic strain measurement of miniature tensile specimens, Exp. Mech. 54 (2) (2014) 165–173.
[50] A. Roschger, S. Gamsjaeger, B. Hofstetter, A. Masic, S. Blouin, P. Messmer, A. Berzlanovich, E.P. Paschalis, P. Roschger, K. Klaushofer, P. Fratzl, Relationship between the v_2PO_4/amide III ratio assessed by Raman spectroscopy and the calcium content measured by quantitative backscattered electron microscopy in healthy human osteonal bone, J. Biomed. Opt. 19 (6) (2014) 065002.
[51] S. Viguet-Carrin, P. Garnero, P.D. Delmas, The role of collagen in bone strength, Osteoporos. Int. 17 (3) (2006) 319–336.
[52] K. Tai, F.J. Ulm, C. Ortiz, Nanogranular origins of the strength of bone, Nano Lett. 6 (11) (2006) 2520–2525.
[53] D.B. Burr, The contribution of the organic matrix to bone's material properties, Bone 31 (1) (2002) 8–11.
[54] T.L. Anderson, Fracture Mechanics: Fundamentals and Applications, 4th Ed., CRC Press, Boca Raton FL, 2017.
[55] H.S. Gupta, W. Wagermaier, G.A. Zickler, D.R. Ben Aroush, S.S. Funari, P. Roschger, H.D. Wagner, P. Fratzl, Nanoscale deformation mechanisms in bone, Nano Lett. 5 (10) (2005) 2108–2111.
[56] J.Y. Rho, G.M. Pharr, Effects of drying on the mechanical properties of bovine femur measured by nanoindentation, J. Mater. Sci. Mater. Med. 10 (8) (1999) 485–488.
[57] Y. Wang, A. Ural, A three-dimensional multiscale finite element model of bone coupling mineralized collagen fibril networks and lamellae, J. Biomech. 112 (2020) 110041.
[58] D.M. Robertson, D. Robertson, C.R. Barrett, Fracture toughness, critical crack length and plastic zone size in bone, J. Biomech. 11 (8–9) (1978) 359–364.
[59] F. Hang, A.H. Barber, Nano-mechanical properties of individual mineralized collagen fibrils from bone tissue, J. R. Soc. Interface 8 (57) (2011) 500–505.
[60] O.L. Katsamenis, H.M.H. Chong, O.G. Andriotis, P.J. Thurner, Load-bearing in cortical bone microstructure: selective stiffening and heterogeneous strain distribution at the lamellar level, J. Mech. Behav. Biomed. Mater. 17 (2013) 152–165.
[61] E.M. Spiesz, P. Roschger, P.K. Zysset, Elastic anisotropy of uniaxial mineralized collagen fibers measured using two-directional indentation. Effects of hydration state and indentation depth, J. Mech. Behav. Biomed. Mater. 12 (2012) 20–28.
[62] O.G. Andriotis, S. Desissaire, P.J. Thurner, Collagen fibrils: nature's highly tunable nonlinear springs, ACS Nano 12 (4) (2018) 3671–3680.
[63] Y.C. Lim, K. Altman, D.F. Farson, K.M. Flores, Micropillar fabrication on bovine cortical bone by direct write femtosecond laser ablation, J. Biomed. Opt. 14 (2009) 064021.
[64] H. Fei, A. Abraham, N. Chawla, H. Jiang, Evaluation of micro-pillar compression tests for accurate determination of elastic-plastic constitutive relations, J. Appl. Mech. 79 (6) (2012) 061011.